Chemical Science

EDGE ARTICLE
Stavros Caratzoulas, Dionisios G. Vlachos *et al.*
Conformations of polyolefins on platinum catalysts
control product distribution in plastics recycling

Conformations of polyolefins on platinum catalysts control product distribution in plastics recycling†

Mehdi Zare,[a] Pavel A. Kots,[a] Stavros Caratzoulas,*[a] and Dionisios G. Vlachos [ID] *[ab]

The design of catalysts for the chemical recycling of plastic waste will benefit greatly from an intimate knowledge of the interfacial polymer–catalyst interactions that determine reactant and product distributions. Here, we investigate backbone chain length, side chain length, and concentration effects on the density and conformation of polyethylene surrogates at the interface with Pt(111) and relate them to experimental product distributions resulting from carbon–carbon bond cleavage. Using replica-exchange molecular dynamics simulations, we characterize the polymer conformations at the interface by the distributions of trains, loops, and tails and their first moments. We find that the preponderance of short chains, in the range of 20 carbon atoms, lies entirely on the Pt surface, whereas longer chains exhibit much broader distributions of conformational features. Remarkably, the average length of trains is independent of the chain length but can be tuned *via* the polymer–surface interaction. Branching profoundly impacts the conformations of long chains at the interface as the distributions of trains become less dispersed and more structured, localized around short trains, with the immediate implication of a wider carbon product distribution upon C–C bond cleavage. The degree of localization increases with the number and size of the side chains. Long chains can adsorb from the melt onto the Pt surface even in melt mixtures containing shorter polymer chains at high concentrations. We confirm experimentally key computational findings and demonstrate that blends may provide a strategy to reduce the selectivity for undesired light gases.

Introduction

Global plastic production has increased exponentially over the last few decades and reached over 400 Mt in 2017 (290 Mt of plastic waste every year).[1] In 2016, 65% of the plastic waste was incinerated or landfilled and only 17% was recycled (16% mechanically and <1% chemically).[2] Mechanical recycling decreases the quality of the product (downcycling) and also requires efficient collection to obtain a homogeneous plastic stream. In contrast, chemical recycling/upcycling can be applied to a wide range of plastics, relieves the pressure on the collection infrastructure, and can yield diverse final products (upcycling).[3–5] For these reasons, catalytic chemical deconstruction has garnered significant attention toward a circular economy (keeping plastic in the economy and out of the environment).[1,6–12]

A main shortcoming and opportunity in the chemical recovery of plastic waste is that its commercialization requires new technologies based on heterogeneous catalysts.[13] To expedite technological developments, it is critical to understand catalyst–plastic interfacial phenomena at the molecular level under reaction conditions. Polyolefins make up a major part of the plastic waste stream and chemical recovery entails catalytic clipping of their backbone; naturally, the product distribution and value depend on the position and number of C–C bonds being cleaved. In other words, the product distribution is determined by the conformation of the polymer on the catalyst.

In this work, we employ replica-exchange molecular dynamics (REMD)[14–17] and the multi-state Bennett acceptance ratio (MBAR)[18] method to sample the conformational space of polymer melts in the adsorbed layer over metal surfaces. We hypothesize that the product carbon distributions obtained experimentally from various feedstocks (low-density polyethylene, LDPE; high-density polyethylene, HDPE; polypropylene, PP; *etc.*), catalysts and reactor residence times are related to the conformations of the adsorbed polymer chains. We study polymer chain length effects by simulating pure C_{20}, C_{26}, C_{44}, C_{71} and C_{142} surrogates of PE melts, and concentration effects by simulating $C_{142}:C_{20}$ mixtures of varying concentrations over Pt(111) at 473 K. We assess and discuss how

aCenter for Plastics Innovation, University of Delaware, 221 Academy Street, Newark, Delaware 19716, USA. E-mail: cstavros@udel.edu; vlachos@udel.edu

bDepartment of Chemical and Biomolecular Engineering, University of Delaware, 150 Academy Street, Newark, Delaware 19716, USA

short-chain polymers forming *via* C–C bond cleavage impact the final product carbon distribution. In addition, we investigate branching effects on the polymer at the catalyst–polymer interface by simulating the C_{71} PE melt backbone branched with methyl, ethyl, and propyl groups. Finally, we discuss the simulation results in the context of our own and previously reported experimental product distributions.

Computational details

Molecular dynamics (MD) simulations were performed using a LAMMPS molecular dynamics simulator.[19] Using the supercell approach, a clean Pt(111) surface was represented by a 12 × 14 slab for short-chain polyethylene (PE) melt simulations (C_{20}, C_{26}, and C_{44}) and by a 15 × 17 slab for long-chain PE melt simulations (C_{71}, C_{144}, mixtures of C_{20} and C_{142}, and C_{71} branched melts). The respective simulation boxes comprise 672 and 1020 Pt atoms. The smaller of the two simulation boxes (used for short-chain melts) has dimensions of 33.24 Å × 33.59 Å × 60.00 Å; the larger of the two (used for long-chain melts) has dimensions of 41.55 Å × 40.79 Å × 75.00 Å. The experimental PE melt density[20] of ∼0.7 g cm^{-3} at 473 K in the middle of the box, which represents bulk PE, was fixed by packing the simulation boxes with the PE chains (see Table S1† for the number of chains used in the simulations). The dimensions of the simulation boxes along the catalyst surface normal were selected so that the PE melt layer will be at least 3 times as large as the equilibrium root-mean-square radius-of-gyration (R_g) of the PE chains in the bulk[21] (see Table S2† for R_g of different PEs calculated in the bulk). The PE melts are exposed to the catalyst surface on one side and vacuum on the other side along the surface normal. All metal atoms were kept fixed during the simulations. The PE melts were initially built using the Moltemplate program package[22] with the OPLS-AA force field[23,24] for PE interactions. The Pt–PE interactions were represented by a Lennard–Jones Pt potential.[25] The LJ cross-term of the intermolecular parameters were calculated by the geometric mixing rules, $\sigma_{ij} = \sqrt{\sigma_i \sigma_j}$ and $\varepsilon_{ij} = \sqrt{\varepsilon_i \varepsilon_j}$. Simulations were carried out in the canonical ensemble (NVT) with the Nosé–Hoover thermostat.[26,27] Electrostatic interactions were accounted for by using a particle–particle particle–mesh (PPPM) method.[28] A 12 Å cutoff radius was used for the van-der-Waals interactions and the transition between short- and long-range electrostatic interactions.

All systems were simulated in three stages. First, the bulk PE melt was equilibrated for 1 ns in the NPT ensemble, followed by a 25 ns NVT ensemble simulation. Next, the equilibrated PE melt was brought to the catalyst surface and the entire system was equilibrated for 25 ns in the NVT ensemble. Finally, the systems were equilibrated for 5 ns using replica-exchange molecular dynamics (REMD) and data were collected for another 10 ns using 9 replicas. Details of the REMD procedures can be found elsewhere.[14–17] The swap between replicas was tried every 10 ps and the snapshots were recorded for each replica every 5 ps. In order to prevent possible drift or rotation of atoms by the temperature corrections, a momentum drift correction was applied every 50 ps.

In the REMD simulations, replicas were selected to obtain a ∼20% acceptance probability of swap moves (P_{acc}) between adjacent replicas, which ensures a free random walk in the temperature space (see Table S3† for temperatures and P_{acc} obtained after each simulation).[15,29] For example, the time series of replica exchange simulation at 473 K, time series of temperature exchange and the total potential energy of the first replica, for the C_{26} melt over Pt(111) are provided in Fig. S1,† indicating a free random walk in the replica and temperature space, respectively. To achieve the optimal temperature distribution that ensures equal P_{acc}, we used the methodology proposed by Rathore *et al.*[30] We used the multi-state Bennet acceptance ratio (MBAR) estimator,[18] implemented in the pymbar program package, to obtain unbiased statistical distributions and averages.

Experimental methods

The Pt/Al_2O_3 catalyst was prepared as follows. Pural SB boehmite (provided by Sasol) was calcined in air at 600 °C to convert it to γ-alumina. A required amount of $[Pt(NH_3)_4](NO_3)_2$ (Sigma-Aldrich) was dissolved in DI water (1.5 g) and added to the Al_2O_3 support at 70 °C. The mixture was stirred with a glass rod for 2 h and then dried overnight at 100 °C in an oven. Subsequently, the sample was heated in pure He at 400 °C for 4 h (ramp rate 2 °C min^{-1}) and then in 20% H_2/He at 300 °C for 2 h.

The solid polymer (PE, Mw ∼4 kDa, Mn ∼1.7 kDa, Sigma-Aldrich) or a mixture of PE and icosane (TCI) was mixed with a freshly reduced catalyst and loaded in a high-pressure stainless-steel Parr reactor with a Teflon magnetic stir bar without a liner. The reactor was sealed, purged with H_2 five times, and then pressurized with 30 bar H_2. Then, the reactor was heated on a hot plate using a band heater for 5 h at 300 °C (ramp rate 10 °C min^{-1}) with magnetic stirring, starting at 110 °C, at 500 rpm setpoint. The reaction temperature was set higher than the simulation temperature. At 300 °C, the adsorbed hydrocarbons react over the Pt surface, allowing us to elucidate how the product distribution is influenced by the binding mode of the polymer or shorter alkane. We focused on low reaction times to form only primary reaction products and avoid extensive secondary hydrogenolysis typical of Pt catalysts.

After the reaction, the reactor was quenched with cold water and ice to 5–6 °C. The gas from the headspace was extracted to a 1 L Tedlar gas bag. The liquid and residual solid in the reactor were mixed with dichloromethane (DCM) solvent (Fisher Scientific) and 20 mg of octacosane (TCI) standard dissolved in DCM. Then the liquid and solid were separated using a Whatman 100 μm filter. The gaseous products were analyzed using a GC-FID with a CP-plot Q 30 m column. Gas standards were used for FID calibration and retention times. The liquid was analyzed on a GC-FID with an HP-1 30 m column using a standard alkane solution for FID calibration. The residual solid was measured gravimetrically. The carbon yield is defined as:

$$\text{Carbon yield of } i\text{th product} = \frac{C_{at} \text{ of } i\text{th product}}{\text{Initial amount of } C_{at}},$$

where C_{at} is the moles of carbon atoms. PE and C_{20} conversions were defined as:

$$PE\ conversion\ =\ \frac{weight\ of\ residual\ solid}{weight\ of\ initial\ PE};$$

$$C_{20}\ conversion\ =\ \frac{mol\ of\ residual\ C_{20}}{initial\ mol\ of\ C_{20}}.$$

When PE was mixed with C_{20}, all residual C_{20} was extracted with excess DCM and analyzed on a GC-FID using an octacosane standard. The residual undissolved C_{20} content in the solid residue was below 5 wt%.

Results and discussion

Analysis of REMD simulations

We used the standard definitions of trains, tails, and loops to analyze the conformations of PE chains on the surface.[31,32] An illustration of these conformational features is given in Fig. 1: contiguous backbone carbon atoms on the surface define a train; two successive trains are connected by a loop, whose carbon atoms do not lie on the surface; and a tail succeeds a train that is not followed by another one. The length of a train, tail, or loop is defined by the number of C–C bonds. These features enable us to statistically predict which and how many C–C bonds lie at the surface and in turn infer the probability of C–C bond cleavage at some position in the chain and thus relate the conformation of the polymer at the catalyst surface to the product distribution. In our analysis, the thickness of the adsorbed layer was defined by the minimum at ~5 Å in the density distribution along the surface normal, as shown in Fig. 2. The sharp peak at 3.2 Å indicates a region of higher-than-bulk density on account of the strong Pt–alkane interactions compared with the competing alkane–alkane interactions. It is evident from $\rho(z)$ and the significant vestigial structure up to about 14 Å that the surface induces a long-range order in the polymer melt; farther away from the surface, the density approaches the bulk value for alkanes at 473 K (~0.7 g cm^{-3}).

Chain length effects

To investigate the dependence of the structural properties of surface adsorbed chains on the length of the PE chain, we simulated C_{20}, C_{26}, C_{44}, C_{71}, and C_{142} melts at 473 K over the Pt(111) surface. Train size, l_{train}, probabilities are plotted in Fig. 3. For short chains (C_{20} and C_{26}), the train distributions
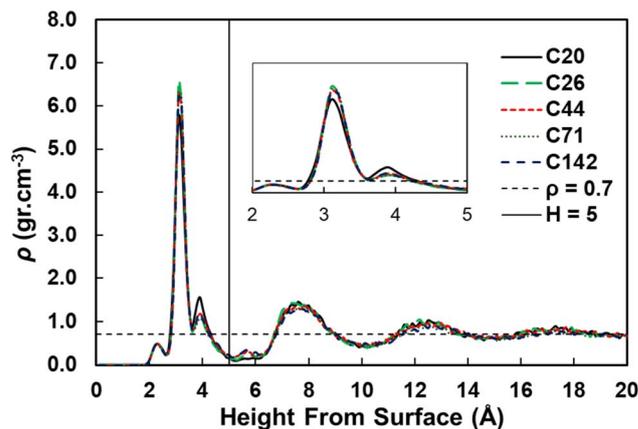

Fig. 2 Density distributions as a function of the distance from the Pt(111) surface for pure PE surrogates. The inset shows the zoom in region from 2 to 5 Å from the surface.

have a significant structure in the sense that they are peaked at l_{train} equal to the size of the chain, namely, the probability of short chains lying entirely on the surface is high. This was also reported by Daoulas *et al.*[21] in a study of the PE melt over graphite and was attributed to the enthalpy gains from full-length adsorption countering the severe entropic penalty associated with constraints on chain propagation in a direction normal to the surface. We should note that the preponderance of chains preferably adsorb with their ends as shown in Fig. S2† where we plot the probability of a chain atom to be leading a train for polymer chains of varying lengths. The distribution in l_{train} becomes less structured and more dispersed with increasing chain size. This is also evident from the cumulative distributions plotted in Fig. 3b. For the C_{71} chain, we calculated probability values of 0.70 for $l_{train} \leq 23$ and 0.22 for $28 \leq l_{train} \leq 37$. For the longer C_{142} chain, we find a large probability of 0.42 for $l_{train} \leq 18$ but also an equally large probability of 0.49 for longer length trains, $20 \leq l_{train} \leq 35$. Despite these differences, the average length of trains, $\bar{l}_{train} \approx 20$, seems to be weakly dependent on the size of the adsorbed chain (see Fig. 4a), a behavior also predicted by the Scheutjens–Fleer lattice theory of polymer adsorption[33,34] in the limit of zero solvent concentration. $\bar{l}_{tail}$ increases monotonically with increasing chain length, also predicted by the Scheutjens–Fleer lattice theory and
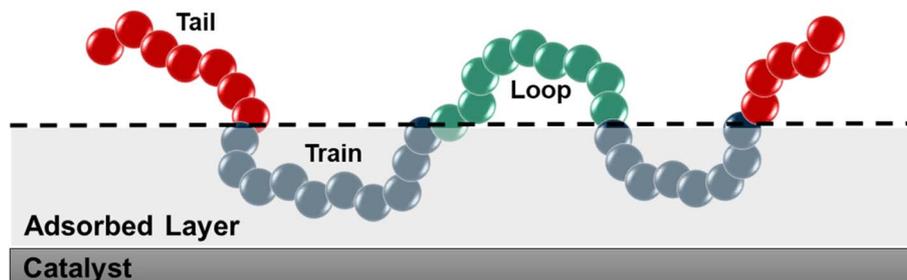

Fig. 1 Schematic representation of trains (blue), tails (red), and loops (green). The thickness of the adsorbed layer was set to 5 Å, which was defined using the density distribution in Fig. 2.

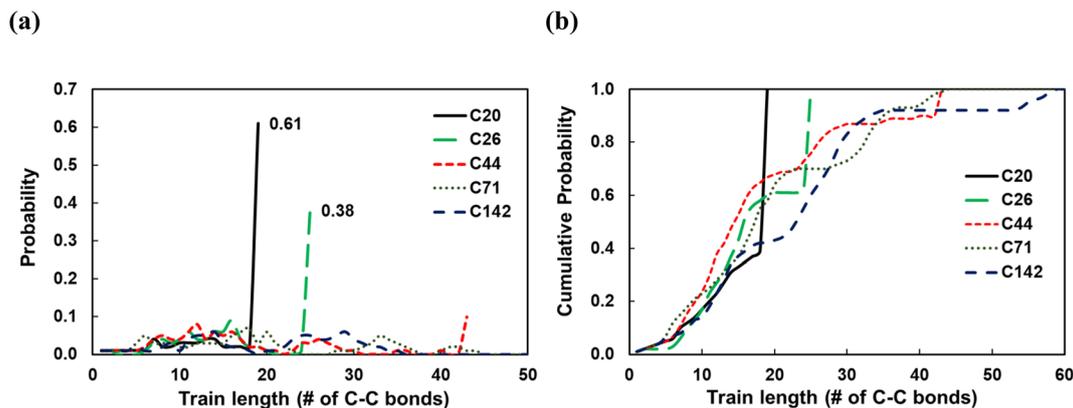**(a)**   **(b)**

Fig. 3 a) Train size probabilities and (b) corresponding cumulative distributions for pure PE melts over Pt(111) at 473 K. Probability of a train length is defined as the fraction of that train among all trains formed.

reported in simulations of the PE melt over a graphite surface.[21,33,34] Consistently, $\bar{t}_{loop} \approx 0$ for short-chain alkanes, while a plateau value of a $\bar{t}_{loop} \approx 20$ is reached for longer chains.

It is instructive to consider the fraction of C–C bonds that belong to trains, tails, and loops (f_{train}, f_{tail}, and f_{loop}); these are shown in Fig. 4b. Most C–C bonds of the adsorbed chains belong to trains for C_{20} ($f_{train} = 0.87$) and C_{26} ($f_{train} = 0.73$) since the chain statistically prefers to be entirely on the surface. Increasing the chain length to C_{44} decreases the dominance of trains sharply, albeit less so for longer chains. Furthermore, most of the C–C bonds of long-chain PE melts belong to tails, but this dominance reaches a plateau for very long chains. We note that the Scheutjens–Fleer lattice theory in the limit of very long chains predicts $f_{tail} = 2/3$, since in polymer adsorption from the melt (i.e., in the limit of zero solvent concentration), nearly two tails are present per molecule, and the remaining 1/3, middle segment of the chain consists of trains and loops. Our simulations show $f_{tail} = 0.74 \pm 0.03$ for the longest chain (C_{142}) studied here, which agrees qualitatively with the lattice theory.

In Fig. 5, we show the results from the conformational analysis of $l_{train} = 20$ trains for the C_{71} and C_{142} chains. In Fig. 5a and b, we plot the average distance of train carbon atoms

from the surface for C_{71} and C_{142}, respectively. With the exception of the two train terminal carbon atoms which interact with the fragments of the polymer chain in the melt, all train carbons are within ~3.3 Å of the Pt surface, indicating that, on average, the trains lie flat on the surface. In Fig. 5c and d, we plot the distribution of the torsion angle, φ, about the 5th, 10th and 15th bonds of the $l_{train} = 20$ train for C_{71} and C_{142}, respectively. For comparison, we also plot the distribution of all torsion angles of the chains in the melt; clearly, the preponderance of conformations is *gauche* or *anti*, $\varphi \approx \pm 70°$ or $\pm 180°$, respectively. The middle of a train, the 10th bond, is primarily in an *anti* conformation, $\varphi \approx \pm 180°$, whereas the two flanking segments, about the 5th and 15th bonds, exhibit greater conformational diversity as we see eclipsed, $\varphi \approx 0°$, as well as *anti* conformations. *Gauche* conformations seem to be rather disfavored and we believe this is because the strong attractive interactions with the metal surface force the polymer to lie flat, presumably overcoming the slightly unfavorable intramolecular interactions which, in the gas phase, are typically relieved by assuming the *gauche* conformation. The distributions are remarkably similar across chain lengths and this makes intuitive sense.
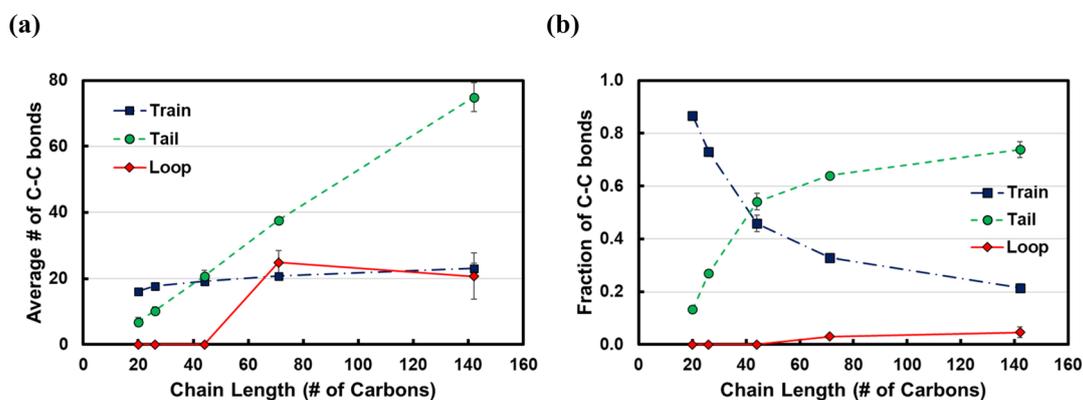
(a)   **(b)**

Fig. 4 (a) Average length of trains, tails and loops in number of carbons and (b) fraction of C−C bonds of adsorbed chains belonging to trains, tails, or loops as a function of the chain length at 473 K. Error bars represent one standard deviation.
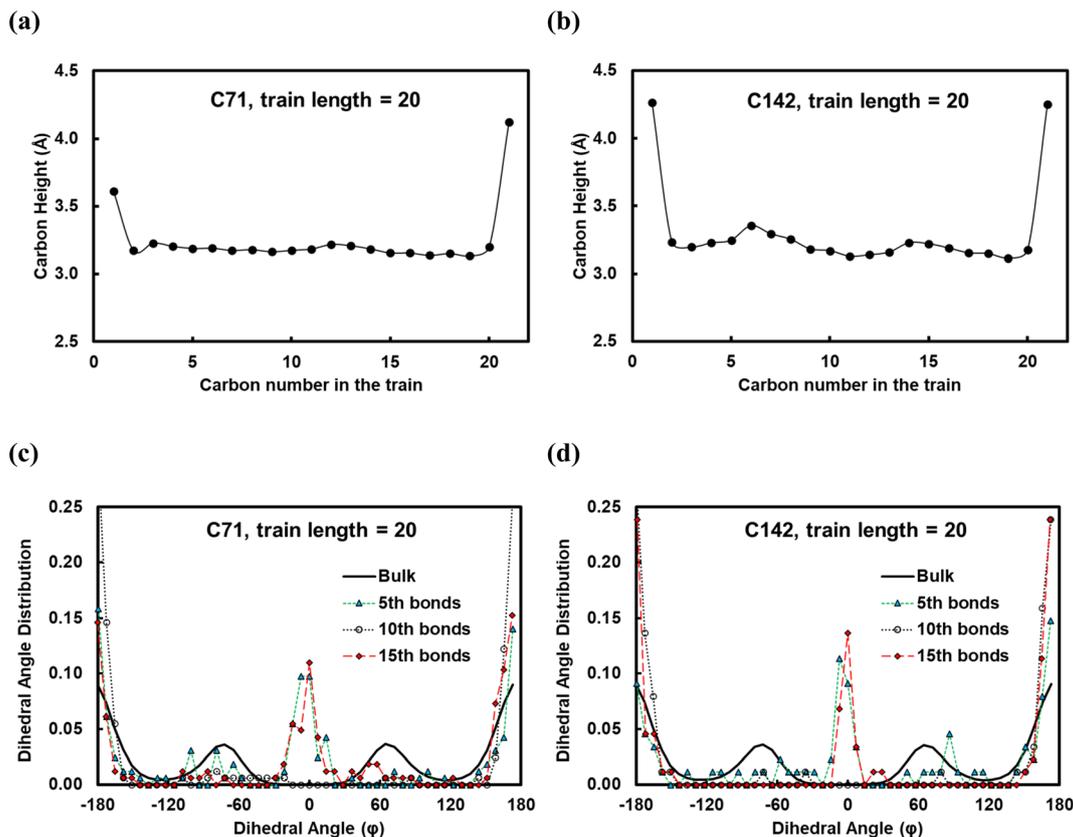
Fig. 5 (a) and (b) Average distance of carbons in a train length of 20 from the Pt(111) surface for the C_{71} and C_{142} melts, respectively. (c) and (d) Distribution of the torsion angle about the 5th, 10th and 15th bonds of the train for the C_{71} and C_{142} melts, respectively.

To investigate the dependence of the results on the Pt potential, we decreased its strength by 50% and reported the data in Fig. S3.† We see similar trends in the average length and fraction of C–C bonds as the chain length increases. However, the longer l_{train} for the weaker potential seems counterintuitive. In this context, we calculated the carbon population up to 6 Å from the surface (see Table S4 and Fig. S4†). We see that the carbon population decreases when the Pt potential becomes weaker. We argue that l_{train} is controlled by the interplay between the surface–alkane and alkane–alkane (lateral) interactions on the surface in that weaker surface–alkane interactions depress the carbon population on the surface and that, in turn, result in longer trains because there is less lateral repulsion from molecules on the surface. These results underscore that product distributions can be controlled by tuning the surface–polymer interactions.

Mixture effects

In practice, the chemical conversion of plastics in a reactor involves a mixture of polymer chains of varying sizes. In addition, the concentration of short chains varies with time as C–C bonds keep breaking at the catalyst surface, which further influences the adsorption of the unreacted polymer and thereby the final product distribution in a batch reactor. To understand how the adsorption geometry of long chains is influenced by shorter ones, we simulated $C_{142}:C_{20}$ binary mixtures containing 27, 50 and 73 wt% of C_{20}. In Fig. 6a and b, we show the corresponding conditional probabilities of train lengths of a given chain identity (belonging either to C_{20} or to C_{142}). Clearly, by having more of C_{20} in the mixture raises the probability of its full-length adsorption ($l_{train} = 19$).

The average train length ($\bar{l}_{train} \approx 20$), shown in Fig. 7a, seems to be insensitive to the C_{20} concentration. Interestingly, the average loop length as a function of C_{20} concentration is flat ($\bar{l}_{loop} \approx 20$) up to 27 wt% C_{20}, goes through a maximum ($\bar{l}_{loop} \approx 50$) at 50 wt% and drops to a value of ~5 at 73 wt% C_{20}. This trend can be explained by the rather broad peak at $l_{loop} \approx 110$ in the conditional distribution corresponding to 50 wt% C_{20}, as shown in Fig. 6c. We argue that at low C_{20} concentration (27 wt%), the surface is less covered by C_{20} molecules, which allows more C_{142} segments on the surface and thus a larger number of short loops should form in C_{142} (see Fig. 7c). Such conformations, however, are inhibited by the increased presence of C_{20} molecules at the surface at medium C_{20} concentration (50 wt%), resulting in fewer yet longer loops ($l_{loop} \approx 100$). At even higher C_{20} concentration (73%), the surface is highly covered in C_{20} and thus the simultaneous adsorption of both ends of C_{142} is inhibited, resulting in conformations without loops. $\bar{l}_{tail}$ decreases almost linearly with increasing C_{20} concentration in the mixture.
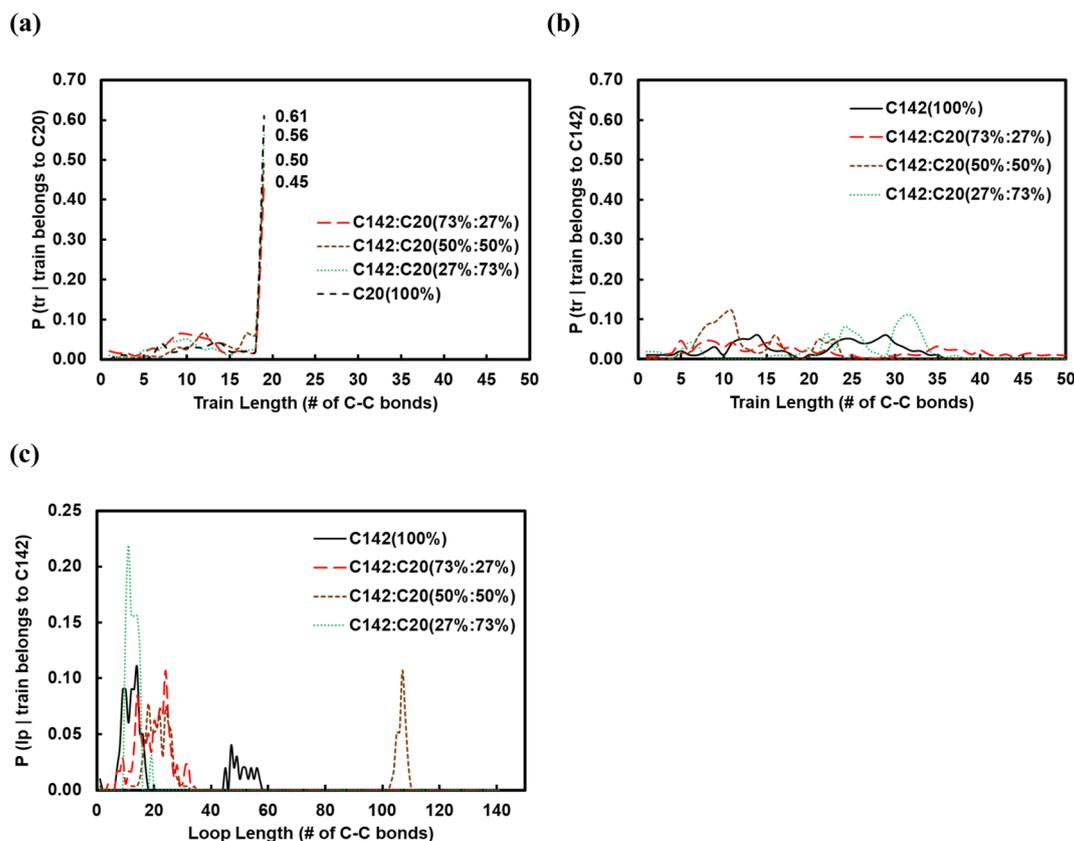
Fig. 6 Conditional probability of the length of the trains in (a) C_{20} chains and (b) C_{142} chains. (c) Conditional probability of the length of the loops in C_{142} for $C_{142}:C_{20}$ mixtures of varying concentrations over Pt(111) at 473 K. Adsorbed C_{20} chains do not form loops.
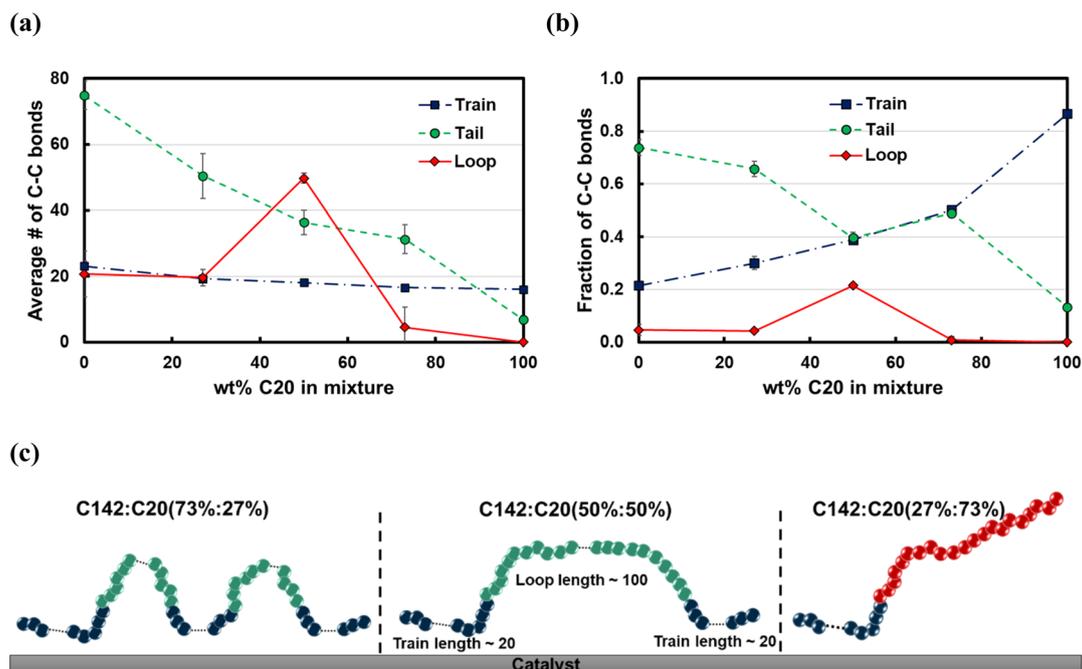

Fig. 7 Effects of C_{20} concentration in binary mixtures of C_{20} and C_{142} over Pt(111) at 473 K on (a) the average length of trains, tails and loops of both C_{20} and C_{142} in the mixture combined, and (b) the fraction of C−C bonds belonging to trains, tails and loops. (c) Cartoons of representative conformations of the C_{142} chain on Pt(111) for $C_{142}:C_{20}$ mixtures of varying C_{20} concentrations. Error bars represent one standard deviation.
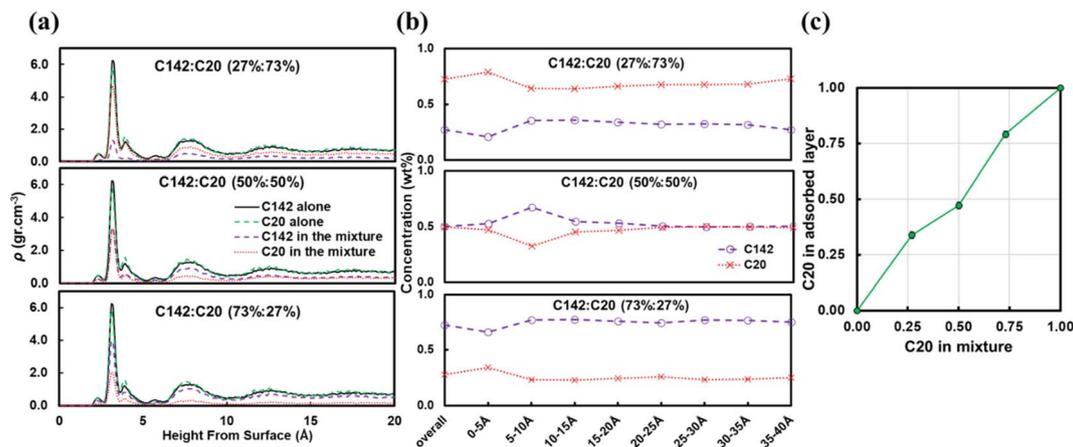
Fig. 8 Mixture effects on (a) the density distributions of the C_{20} and C_{142} PE melts, and (b) the carbon concentrations of C_{20} and C_{142} within layers of same volume and thickness Δz at different positions along the surface normal of Pt(111) at 473 K. (c) C_{20} concentration in the adsorbed layer (within 5 Å of the surface) in different mixtures, indicating that the C_{142} PE chains can still adsorb and be cleaved, even at high C_{20} concentrations.

Fig. 7b presents the fraction f_{train} for mixtures. It is monotonically increasing with the C_{20} concentration, giving additional evidence of favorable adsorption of C_{20}. The increase in f_{tail} at 73 wt% C_{20} is attributed to the absence of loops at high C_{20} concentration since the surface is mostly covered in C_{20}. Also, the maximum in f_{loop} at 50 wt% is aligned with the formation of longer loops observed in Fig. 6c and 7c. Fig. 8 presents the density distribution and carbon concentration of the mixtures at different positions along the surface normal. The carbon concentration in the adsorbed layer seems to be independent of the C_{20} concentration and almost the same as in the bulk. This highlights that long chains can reach the surface and be cleaved/converted even at high concentrations of shorter chains. This agrees with experimental findings by Celik *et al.*[10]
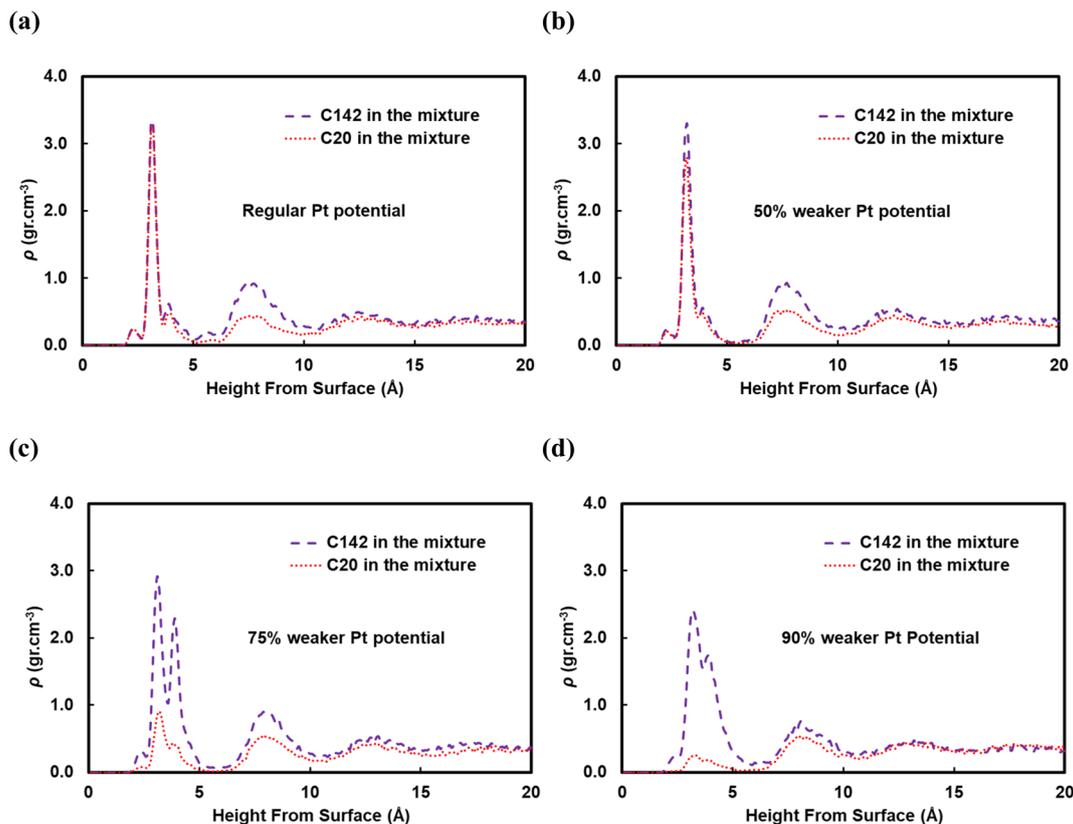

Fig. 9 Density profiles of a binary mixture of C_{20} and C_{142} with 50 wt% C_{20} for a (a) regular, (b) 50% weaker, (c) 75% weaker, and (d) 90% weaker Pt potential showing long chain segregations by decreasing the Pt potential strength.

for PE upcycling over a $Pt/SrTiO_3$ catalyst and the observed decrease in dispersity ($Đ = M_w/M_n$) with increasing reaction time, suggesting the preferential adsorption and cleavage of longer chains. On the other hand, favorable adsorption and cleavage of lighter molecules would result in increasing $Đ$ with time as the lighter chains undergo hydrogenolysis to even shorter chains. The decreasing $Đ$ with reaction time was also observed in a previous study of ours investigating isotactic polypropylene (i-PP) hydrogenolysis over Ru/TiO_2.[7] These observations also show that C–C bond breaking in a very polydisperse polymer leads to a narrower distribution due to consumption of heavier chains.

A reviewer of our manuscript brought to our attention that, in polymer blends, segregation of one of the components to the surface is possible. Yethiraj *et al.*[35] have studied the behavior near a noninteracting solid surface of a binary blend with one component being stiffer than the other. They suggested that, at melt-like densities, the stiff chains accumulate at the surface more than the flexible ones do. It has been suggested[36] that the observed segregation[37,38] is caused by differences in packing and that the surface segregation is a strong function of the relative polymer–polymer and polymer–surface interactions; due to entropic confinement, long chains near weakly attractive surfaces prefer to diffuse away but strong polymer–surface attractive interactions can compensate for the entropic cost. We

have investigated this behavior for our system and in Fig. 9 we plot density profiles for the 50 : 50 wt% C_{20} : C_{142} binary mixture for four cases: the "full" Pt–polymer potential (Fig. 9a) and three potentials in which the Pt–polymer interactions are progressively reduced by 50, 75 and 90% (Fig. 9b, c and d, respectively). Under the full-strength potential, there is no difference between the long and short chains in terms of their preferential segregation at the surface (Fig. 9a). The progressive weakening of the surface–polymer potential, however, seems to affect both the C_{20} and C_{142} chains, in the sense that the density peaks at $z < 5$ Å become more diffuse and less intense, but more so the former. This is an intriguing deviation from Yethiraj[36] and warrants further investigation in future work.

Branching effects

Commercial polyethylene, such as HDPE and LDPE, is a branched molecule endowed with different properties from linear alkanes. To study the effects of branching on the polymer backbone, we considered the C_{71} alkane and introduced 7 or 13 methyl, ethyl, propyl groups in the backbone; the branches were equally spaced along the chain. From the train and loop size distributions shown in Fig. 10a and b and specifically the sharp peaks at small l_{train} and l_{loop} values, we conclude that branching promotes polymer bending around branched carbons and that shorter trains and loops form on increasing the number of
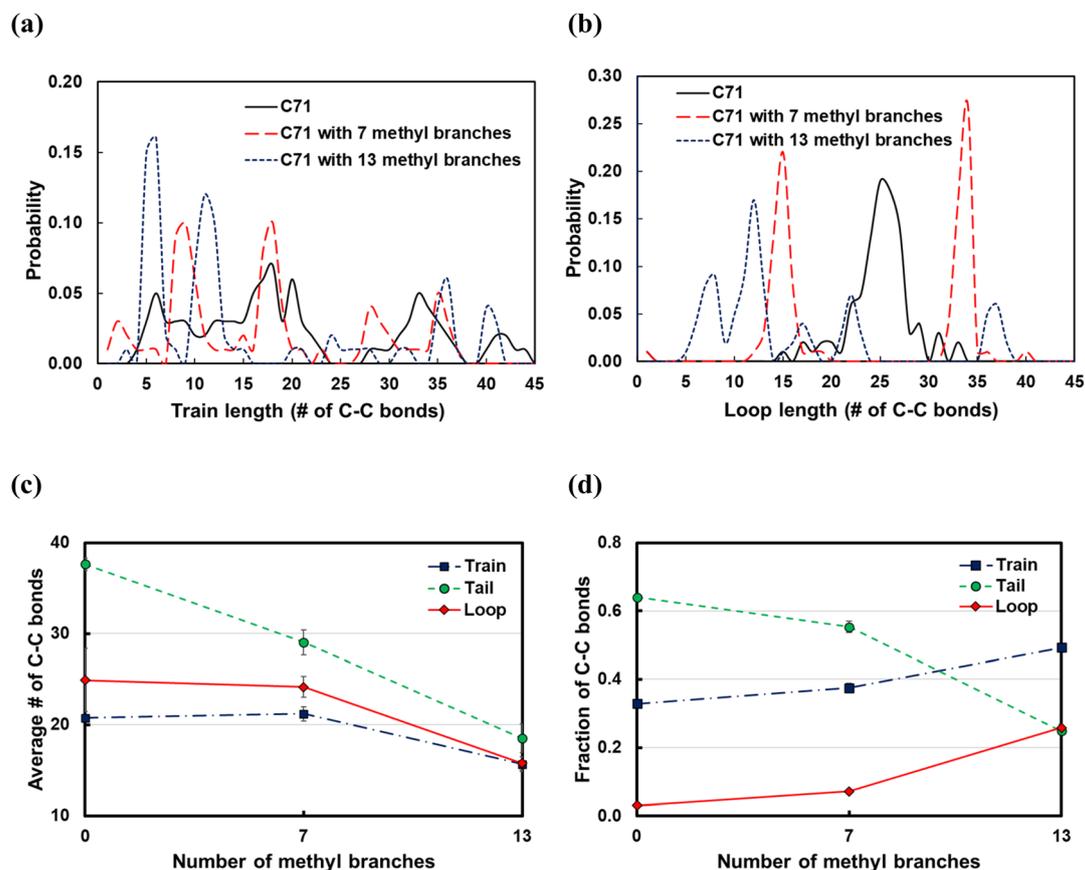

Fig. 10 Dependence of (a) train size distributions, (b) loop size distributions, (c) average length of trains, tails, and loops, and (d) fraction of C–C bonds in trains, tails or loops on the number of methyl side chains in the C_{71} backbone. Error bars represent one standard deviation.

branches. As a result, as shown in Fig. 10d, the fraction of C–C bonds in trains and loops increases, and the fraction of those in tails drops. Also, $\bar{l}_{train}$ and $\bar{l}_{loop}$ do not vary when we add 7 methyl branches, but they are distributed with sharp peaks at the branching points (see Fig. 10a and b). However, $\bar{l}_{train}$ and $\bar{l}_{loop}$ decrease when we add 13 methyl branches. $\bar{l}_{tail}$ decreases independently of the number of branches because the number of loops and trains increases. In summary, we argue that the favorable bending of the polymer around branched points can lead to a wider product distribution since different segments of the polymer can adsorb on the surface and be susceptible to C–

C scissions at different positions. This agrees with previous experimental work in which hydrocracking of different polyolefin feedstocks over Pt/WO$_3$/ZrO$_2$ mixed with HY zeolite resulted in a wider product distribution of PP compared to PE feedstocks.[6]

Fig. 11 displays the effect of the side chain length on the structural properties of the C$_{71}$ PE melt over the Pt(111) surface. Introducing the methyl branches in the C$_{71}$ backbone forms more trains (short or long; see Fig. 11a and e) and loops (short or long; see Fig. 11b and e), so thereby shorter tails (see Fig. 11d). Replacing methyl side chains with ethyl groups results
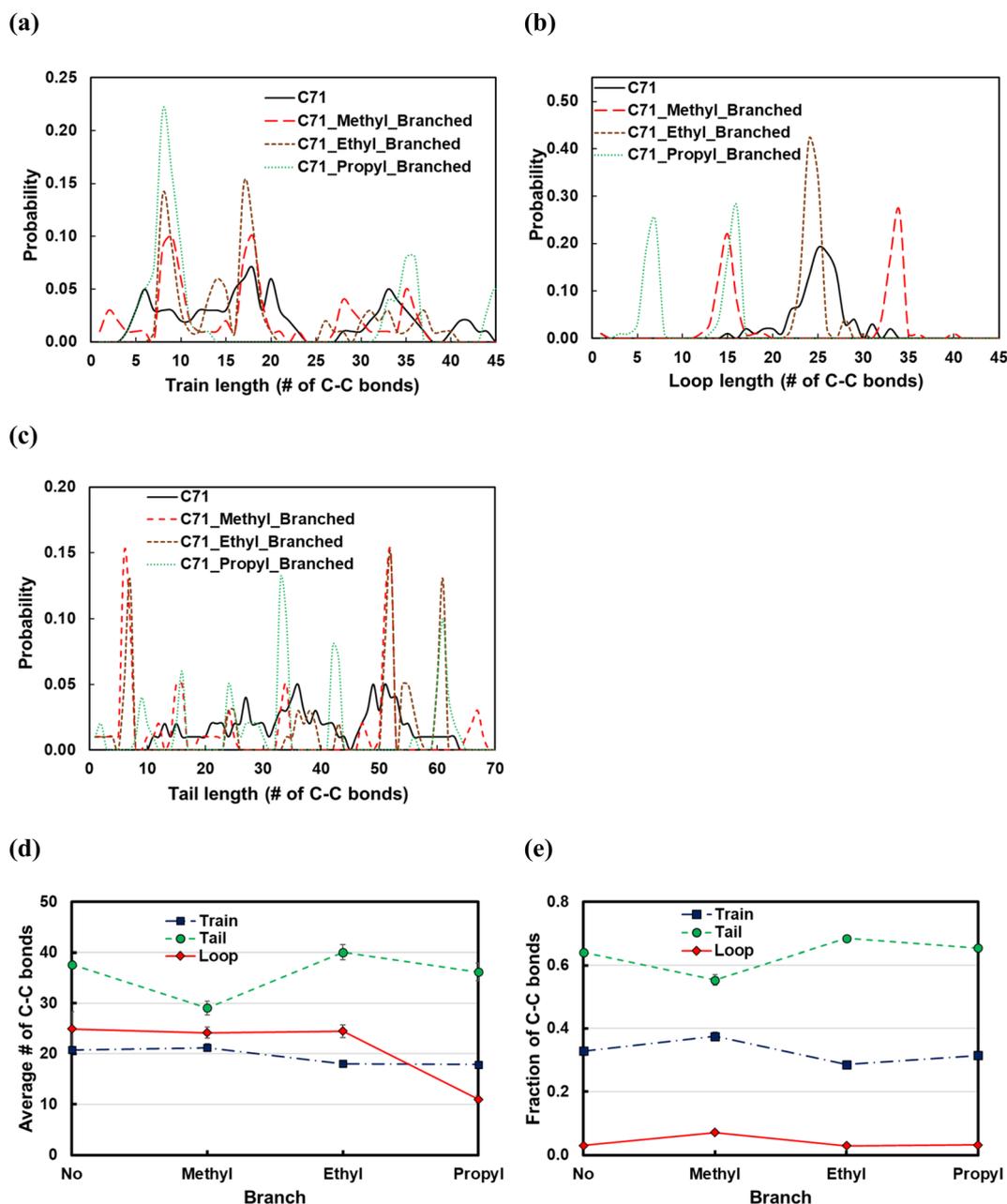

Fig. 11 Dependence of (a) train size distributions, (b) loop size distributions, (c) tail size distributions, (d) average length of trains, tails, and loops, and (e) fraction of C–C bonds in trains, tails, or loops on the length of side chains in the C$_{71}$ backbone. Error bars represent one standard deviation.

in longer tails (new peak at $l_{\text{tail}} = 60$ in Fig. 11c), shorter trains (larger peaks at $l_{\text{train}} = 9$ and 18 in Fig. 11b), and hence longer loops (large peak at $l_{\text{loop}} = 25$ in Fig. 11b). Increasing the side chain length from ethyl to propyl results in formation of more loops of shorter length (peaks shift to the left in Fig. 11b), more yet shorter trains (large peak at $l_{\text{train}} = 9$ in Fig. 11a), and thereby fewer tails of shorter size (see Fig. 11d). In summary, the longer the side chain, the more the loops and trains, and the fewer the tails, whose lengths are determined by the interactions between the side chains and the polymer bulk at the interface with the adsorbed layer. However, the effect for the small side chains studied is slight.

Experimental results on the effect of C_{20} in polyethylene decomposition over Pt

The polymer binding to the metal surface affects the C–C bond hydrogenolysis. To further elaborate on this point, we performed experiments with pure PE over Pt/Al_2O_3 catalysts at high Pt loading (6.4 wt%). This catalyst is active in PE hydrogenolysis, giving a broad distribution of liquid products and some light gases.[10] High Pt loading ensures the formation of relatively large particles, making experimental results more relatable to the modeling. Pure PE converts to a broad distribution of C_1–C_{35} n-alkanes, at 16% conversion in 5 h (Fig. 12). The relatively high yields of light C_1–C_5 products are consistent with previous reports.[10] When a mixture of PE and C_{20} reacts over Pt/Al_2O_3, the

product distribution changes: the proportion of C_1–C_4 decreases while that of C_{11}–C_{19} and of heavy C_{21+} increases. The conversion of PE and C_{20} reached 19 and 38%, respectively, from which we infer that additional C_{11}–C_{19} products form via C–C bond breaking in C_{20} rather than in PE. Therefore, PE and C_{20} have comparable reactivities, each generating its own set of products, albeit with some overlap. This is consistent with the MD predictions that PE and the shorter molecules do not mutually exclude each other from the Pt surface, and that the PE/C_{20} ratio in the adsorbed layer is similar to that in the bulk.

Interestingly, the addition of C_{20} reduces the yield of light gases. The latter probably originate from secondary hydrogenolysis of longer initial intermediates, as shown in recent work regarding ruthenium.[8] C_{20} substitutes part of PE on the Pt surface, reducing secondary PE hydrogenolysis products. Indeed, this explanation agrees with experiments (Fig. 12) and the MD simulations, which show that C_{20} dramatically changes the conformation of adsorbed PE. According to the simulations (Fig. 6 and 7), short alkanes cause longer PE loops. Long trains appear to be a prerequisite for deep hydrogenolysis to C_1–C_4 products, while long loops and tails limit the reactivity to liquid C_{10+}. This selectivity-altering approach is an intriguing way to generate more valuable (liquid) products from PE and avoid light gases.

Conclusions

In this work, we have employed replica-exchange molecular dynamics simulations to characterize the conformational spaces of C_{20}, C_{26}, C_{44}, C_{71}, and C_{142} pure melts and C_{142} : C_{20} binary mixtures of varying concentrations at the interface with Pt(111) by the distributions of trains, loops, and tails and their first moments. Our analysis shows that the preponderance of short chains, in the range of 20 carbon atoms, lies entirely on the Pt surface as the enthalpic gains seem to outweigh the entropic gains associated with propagation of the chains in the direction normal to the surface. On the other hand, longer chains exhibit much broader distributions of all three conformational features. Remarkably, the average length of trains seems to be quite independent of the size of the alkane chain. Branching has a profound effect on the conformations of long chains at the interface as the favorable bending of the polymer around branched points at the surface results in train distributions that are less dispersed and more structured, and localized around short-trains, with the immediate implication of a wider carbon product distribution upon C–C bond cleavage. The degree of localization increases with the number and size of the side chains. Long chains can adsorb from the melt onto the Pt surface even in melt mixtures containing shorter polymer chains at high concentrations. This was further confirmed by experiments which showed comparable reactivity of PE and the C_{20} alkane. Computational results of a binary mixture of C_{142} and C_{20} with various concentrations reveal that both long and short chains can adsorb on the Pt catalyst surface for C–C scission even at high concentrations of the short chains. This observation is in line with the very high dispersity ($Đ$) of reaction products derived from PE over Pt/Al_2O_3 in prior work.[10]
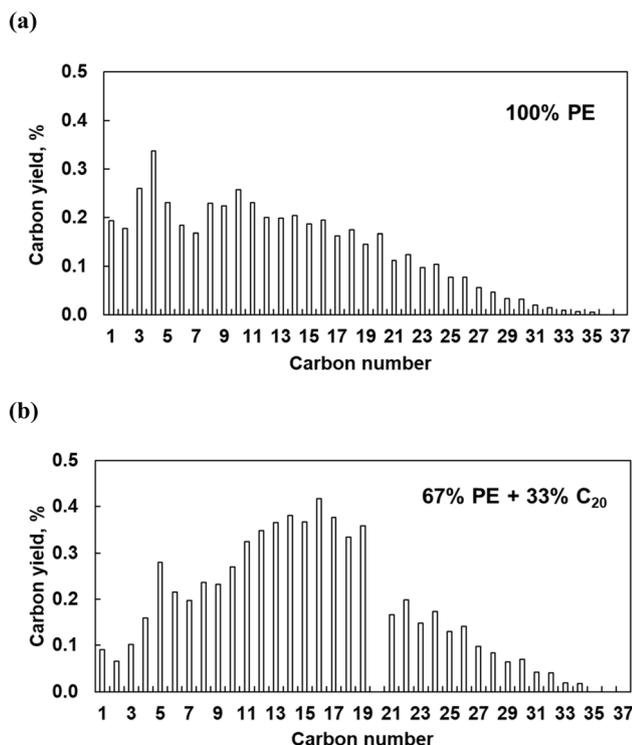

Fig. 12 Carbon yield as a function of the product carbon number for liquid and gaseous products formed from pure PE (a) and PE mixed with C_{20} n-alkane in a 67 : 33 wt% proportion (b). Reaction conditions: 300 °C, 30 bar H_2, 5 h reaction time, 6.4% Pt/Al_2O_3 0.1 g, 2 g PE or 1.32 g PE mixed with 0.67 g C_{20}.

Also, C_{20} addition alters the conformation of C_{142} on the surface, which in turn impacts reactivity. This agrees qualitatively with the formation of fewer light products (C_1–C_4 alkanes) when PE is mixed with C_{20} in the experiments, and may provide a new strategy to minimize light gases by minimizing the accessible catalyst sites. The interaction of the polymer with the surface also alters the train size, with weaker interactions leading to longer trains, and can similarly be leveraged to tune the product distribution. The quantitative relation between the structural properties of polymer chains on the surface and the experimental product distribution remains the subject of future work.

Data availability

Datasets used for the analyses presented in this article are provided as ESI.†

Author contributions

M. Z. performed all calculations and analysis. P. A. K. performed the experiments and associated analysis. S. C. and D. G. V. conceived the overall idea, supervised the project, and obtained the funding. The manuscript was written by M. Z. and S. C. with input from all the authors.

Conflicts of interest

The authors declare no conflict of interests.

Acknowledgements

References

1 M. Tsakona, E. Baker, I. Rucevska, T. Maes, L. R. Appelquist, M. Macmillan-Lawler, P. Harris, K. Raubenheimer, R. Langeard, H. Savelli-Soderberg, K. O. Woodall, J. Dittkrist, T. A. Zwimpfer, R. Aidis, C. Mafuta and T. Schoolmeester, *Drowning in Plastics–Marine Litter and Plastic Waste Vital Graphics*, United Nations Environment Programme, 2021.

2 R. Geyer, *Plastic Waste and Recycling*, ed. T. M. Letcher, Academic Press, 2020, DOI: 10.1016/B978-0-12-817880-5.00002-5, pp. 13–32.

3 N. Singh, D. Hui, R. Singh, I. P. S. Ahuja, L. Feo and F. Fraternali, *Composites, Part B*, 2017, **115**, 409–422.

4 M. Solis and S. Silveira, *Waste Manage.*, 2020, **105**, 128–138.

5 T. Thiounn and R. C. Smith, *J. Polym. Sci.*, 2020, **58**, 1347–1364.

6 S. Liu, P. A. Kots, B. C. Vance, A. Danielson and D. G. Vlachos, *Sci. Adv.*, 2021, **7**, eabf8283.

7 P. A. Kots, S. Liu, B. C. Vance, C. Wang, J. D. Sheehan and D. G. Vlachos, *ACS Catal.*, 2021, **11**, 8104–8115.

8 C. Wang, T. Xie, P. A. Kots, B. C. Vance, K. Yu, P. Kumar, J. Fu, S. Liu, G. Tsilomelekis, E. A. Stach, W. Zheng and D. G. Vlachos, *JACS Au*, 2021, **1**, 1422–1434.

9 A. Tennakoon, X. Wu, A. L. Paterson, S. Patnaik, Y. Pei, A. M. LaPointe, S. C. Ammal, R. A. Hackler, A. Heyden, I. I. Slowing, G. W. Coates, M. Delferro, B. Peters, W. Huang, A. D. Sadow and F. A. Perras, *Nat. Catal.*, 2020, **3**, 893–901.

10 G. Celik, R. M. Kennedy, R. A. Hackler, M. Ferrandon, A. Tennakoon, S. Patnaik, A. M. LaPointe, S. C. Ammal, A. Heyden, F. A. Perras, M. Pruski, S. L. Scott, K. R. Poeppelmeier, A. D. Sadow and M. Delferro, *ACS Cent. Sci.*, 2019, **5**, 1795–1803.

11 F. Zhang, M. Zeng, R. D. Yappert, J. Sun, Y.-H. Lee, A. M. LaPointe, B. Peters, M. M. Abu-Omar and S. L. Scott, *Science*, 2020, **370**, 437–441.

12 B. C. Vance, P. A. Kots, C. Wang, Z. R. Hinton, C. M. Quinn, T. H. Epps, L. T. J. Korley and D. G. Vlachos, *Appl. Catal., B*, 2021, **299**, 120483.

13 P. A. Kots, B. C. Vance and D. G. Vlachos, *React. Chem. Eng.*, 2022, **7**, 41–54.

14 K. Hukushima and K. Nemoto, *J. Phys. Soc. Jpn.*, 1996, **65**, 1604–1608.

15 Y. Sugita and Y. Okamoto, *Chem. Phys. Lett.*, 1999, **314**, 141–151.

16 Y. Sugita, A. Kitao and Y. Okamoto, *J. Chem. Phys.*, 2000, **113**, 6042–6051.

17 D. J. Earl and M. W. Deem, *Phys. Chem. Chem. Phys.*, 2005, **7**, 3910–3916.

18 M. R. Shirts and J. D. Chodera, *J. Chem. Phys.*, 2008, **129**, 124105.

19 A. P. Thompson, H. M. Aktulga, R. Berger, D. S. Bolintineanu, W. M. Brown, P. S. Crozier, P. J. in 't Veld, A. Kohlmeyer, S. G. Moore, T. D. Nguyen, R. Shan, M. J. Stevens, J. Tranchida, C. Trott and S. J. Plimpton, *Comput. Phys. Commun.*, 2022, **271**, 108171.

20 G. T. Dee, T. Ougizawa and D. J. Walsh, *Polymer*, 1992, **33**, 3462–3469.

21 K. C. Daoulas, V. A. Harmandaris and V. G. Mavrantzas, *Macromolecules*, 2005, **38**, 5780–5795.

22 A. I. Jewett, D. Stelter, J. Lambert, S. M. Saladi, O. M. Roscioni, M. Ricci, L. Autin, M. Maritan, S. M. Bashusqeh, T. Keyes, R. T. Dame, J.-E. Shea, G. J. Jensen and D. S. Goodsell, *J. Mol. Biol.*, 2021, **433**, 166841.

23 W. L. Jorgensen and J. Tirado-Rives, *J. Comput. Chem.*, 2005, **26**, 1689–1700.

24 J. A. Rackers, Z. Wang, C. Lu, M. L. Laury, L. Lagardère, M. J. Schnieders, J.-P. Piquemal, P. Ren and J. W. Ponder, *J. Chem. Theory Comput.*, 2018, **14**, 5273–5289.

25 H. Heinz, R. A. Vaia, B. L. Farmer and R. R. Naik, *J. Phys. Chem. C*, 2008, **112**, 17281–17290.

26 S. Nosé, *J. Chem. Phys.*, 1984, **81**, 511–519.

27 W. G. Hoover, *Phys. Rev. A*, 1985, **31**, 1695–1697.

28 R. W. Hockney and J. W. Eastwood, *Computer Simulation Using Particles*, Adam Hilger, New York 1989.

29 A. Kone and D. A. Kofke, *J. Chem. Phys.*, 2005, **122**, 206101.

30 N. Rathore, M. Chopra and J. J. d. Pablo, *J. Chem. Phys.*, 2005, **122**, 024111.

31 A. N. Semenov, J. Bonet-Avalos, A. Johner and J. F. Joanny, *Macromolecules*, 1996, **29**, 2179–2196.

32 C. A. J. Hoeve, E. A. DiMarzio and P. Peyser, *J. Chem. Phys.*, 1965, **42**, 2558–2563.

33 J. M. H. M. Scheutjens and G. J. Fleer, *J. Phys. Chem.*, 1979, **83**, 1619–1635.

34 G. J. Fleer, J. M. H. M. Scheutjens and M. A. C. Stuart, *Colloids Surf.*, 1988, **31**, 1–29.

35 A. Yethiraj, S. Kumar, A. Hariharan and K. S. Schweizer, *J. Chem. Phys.*, 1994, **100**, 4691–4694.

36 A. Yethiraj, *Phys. Rev. Lett.*, 1995, **74**, 2018–2021.

37 U. Steiner, J. Klein, E. Eiser, A. Budkowski and L. J. Fetters, *Science*, 1992, **258**, 1126–1129.

38 M. Sikka, N. Singh, A. Karim, F. S. Bates, S. K. Satija and C. F. Majkrzak, *Phys. Rev. Lett.*, 1993, **70**, 307–310.